



50-year Wind Speed Maps for Tropical Cyclone-affected Regions using Best Track data

Keeta Chapman-Smith¹, Xiaoli Guo Larsén¹, and Mark Laier Brodersen²

¹Department of Wind and Energy Systems, Technical University of Denmark, Risø Campus, Roskilde, Denmark

²Ørsted Wind Power, Gentofte, Denmark

Correspondence: Keeta Chapman-Smith (kechap@dtu.dk)

Abstract. Accurate estimation of extreme wind speeds from tropical cyclones is a significant challenge within tropical cyclone prone regions. This study presents a method to estimate the 50-year return wind speed at heights relevant to wind turbines. The International Best Track Archive for Climate Stewardship data is combined with the Holland parametric model and the Gumbel distribution to assess extreme winds within three tropical cyclone-affected regions within the Northern Hemisphere.

5 These regions are Taiwan, Japan, and the east coast of the United States of America. To assess the uncertainty within the results from differing input parameters, Monte Carlo simulations are used. The method performs well in Taiwan and Japan which can be attributed to the large sample size of data points located within a limited spatial area. The east coast of the United States performs less well, which conversely, is due to the smaller sample size and wider spatial region of which they cover. This study shows that combining International Best Track Archive for Climate Stewardship data with parametric and statistical models
10 provides a practical approach to estimate extreme wind speeds while highlighting the need for an understanding of regional characteristics to ensure reliability of the results.

1 Introduction

Tropical cyclones (TCs) can be a devastating weather event, especially in coastal and offshore regions (Mortlock et al., 2018). Therefore, assessment of extreme winds is increasingly important due to the current a global expansion of offshore infrastructure, including offshore wind farms (Chen and Su, 2022).

The International Electrotechnical Commission (IEC), within standard 61400-1, provides a reference wind speed class specifically for wind turbines in TC-prone regions, known as Class T (Commission, 2019). However, it also expresses that the reference wind speed may not cover all regions prone to TCs.

There are a range of methods that have been used within previous studies to assess extreme wind speeds from TCs. For 20 example, many have taken advantage of the International Best Track Archive for Climate Stewardship (IBTrACS) (Knapp et al., 2010; Gahtan et al., 2024). IBTrACS is a state-of-the-art dataset containing information on TC parameters such as the maximum wind speed, minimum sea level pressure, centre position, radius of maximum winds (RMW). IBTrACS is widely known and used. Of those using the IBTrACS dataset, select studies, such as (Ott, 2006; Schreck et al., 2014; Kossin, 2018)



25 focus on general TC analysis, whereas, others such as (Bloemendaal et al., 2020b; Morin et al., 2024; Xu et al., 2024) focus on the combination of IBTrACS with other datasets to develop new synthetic datasets.

The IBTrACS dataset, however, is not without its limitations. IBTrACS does not provide the entire wind field but rather a singular value for the maximum wind speed at each given time step. To obtain the entire wind field, parametric models, such as the Holland Model (Holland, 1980), can be implemented to extrapolate a singular point into a wind field in a computationally efficient way. Parametric models are used across academic and industrial fields to investigate TCs (Arthur, 2021) and the 30 combination of IBTrACS data with parametric models is a well used method (Ott, 2006; Fang et al., 2020; Wei et al., 2023).

In an attempt to mitigate the damage caused by extreme winds, the IEC standard defines a reference speed for each class of wind turbine. The reference speed is defined as the 10-minute wind speed average for a return period of 50 years (U_{50}) at turbine hub height. To align with the IEC standard, this paper focuses on these exact requirements. To calculate U_{50} , Generalised Extreme Value (GEV) is implemented, as previously used by Abild (1994); Larsén et al. (2015).

35 TC's U_{50} has previously been studied, but they have rather focussed on using reanalysis data, or combining IBTrACS reanalysis data with IBTrACS (Anastasiades and McSharry, 2014), combining IBTrACS with more complex models to generate a synthetic dataset (Vickery et al., 2009; Bloemendaal et al., 2020a), or comparing extreme value analysis methods for TCs (Ott, 2006; Kong et al., 2024). Reanalysis datasets can provide useful information on TCs (Kossin, 2015) and other weather phenomena (Mavromatis, 2022; Wang et al., 2023), but they often underestimate the maximum wind speeds of TCs (Li et al., 40 2024), making it difficult to estimate the potential impact of TCs on offshore infrastructure (Gandoi and Garza, 2024; Liu et al., 2025). Another commonality between previous studies is the primary focus on either a single basin for winds at 10 m (Ott, 2006; Kong et al., 2024) or a limited number of specific latitude-longitude coordinates (Vickery et al., 2009; Bloemendaal et al., 2020a).

45 One particular study, Larsén and Ott (2022), focussed on overcoming the systematic underestimation of extreme TC wind speed within reanalysis data. The missing wind variability was filled in within the Climate Forecast System Reanalysis (CFSR) reanalysis data using a spectral correction method. The application of the spectral correction uses the U_{50} estimation from Ott (2006), which in turn is based upon using the Japanese Meteorological Agency (JMA) track data (a subset of the IBTrACS dataset). This method was applied to two regions: the southwest of the northern Pacific Ocean and the western Atlantic Ocean, and, later adjusted in Imberger et al. (2024) to include two more reanalysis datasets, ERA5 [European Centre for Medium-50 Range Weather Forecast Reanalysis v5] and MERRA 2 [Modern-Era Retrospective analysis for Research and Applications] for where IBTrACS data is available. However, this study presents no validation through measurements.

This paper focuses on the use of the state-of-the-art IBTrACS data, updates the study of Ott (2006) which was only over the Typhoon affected southwest of the northern Pacific ocean. The regions to extended to include: the ocean around Taiwan located in the Western Pacific, the ocean around Japan also located in the Western Pacific and the east coast of the United States of 55 America (ECUS) located in the Northern Atlantic. These have been chosen as they encompass most of the regions affected by TCs in the Northern Hemisphere and areas contain offshore wind development.

The aim of this study is, first of all, to develop a computationally efficient method to derive U_{50} that can be applied across many different regions, taking advantage of the IBTrACS data. Secondly, this study investigates the applicability of the IB-



TrACS data in different regions for the calculation of U_{50} by recognising regional TC characteristics. Thirdly, this study
60 explicitly accounts for how uncertainties within IBTrACS propagate through to the final U_{50} results. This paper is a necessary
complement to Ott (2006) with its more complete use of IBTrACS data, and to Larsén and Ott (2022) and Imberger et al.
(2024) due to the use of IBTrACS data.

Section 2 introduces the method developed to estimate U_{50} and the accompanying uncertainty analysis using Monte Carlo
simulations. Results are presented in Section 3, the uncertainty analysis is detailed in Section 4, followed by Discussions and
65 Conclusions in Section 5 and 6, respectively. A list for abbreviation is provided in the Appendix for readability.

2 Method

This section will introduce and discuss the data used within the analysis and the method by which the data has been processed
to obtain U_{50} in three regions.

Below is a brief overview of the steps taken to calculate U_{50} . Each step is explained in more detail in the corresponding
70 sections throughout the paper. Figure 1 shows the workflow of the method.

1. **Define the regions of interest:** The three regions of focus are: Taiwan, Japan, and ECUS. The exact coordinates used to
define these regions are described in Section 2.2.
2. **Select relevant data:** A set of data restrictions is applied to the IBTrACS data. These restrictions are (1) the data point
must fall within the region of interest, (2) the data point contain either the radius of maximum wind (RMW) or the 50 kt
75 radius, the minimum sea-level pressure and maximum wind speed and (3) the data point is over ocean. (2) is required
as they are the necessary parameter inputs to the parametric model, and (3) is required as the parametric model used to
extrapolate a single data point to a wind field is only valid over ocean. The parametric model is discussed in point 4.
3. **Convert wind speeds to common averaging period:** The IBTrACS dataset is a compilation of data from agencies
across the globe. Hence, the maximum wind speed is given at different averaging periods. All wind speeds are converted
80 to a 10-minute averaging period using the method described in Harper et al. (2010). The 10-minute average was chosen
as it is used as the reference speed at hub height within the IEC standard 61400-1 (Commission, 2019). Details of this
conversion process are provided in Section 2.3.
4. **The Holland model:** A $0.25^\circ \times 0.25^\circ$ latitude-longitude grid is defined. The grid was defined to be this resolution,
as a higher resolution grid requires larger computational resources, and a lower resolution could dilute key features of
85 U_{50} . Once the grid is defined, the Holland model can be used. Using input parameters such as wind speed and RMW,
the Holland model can extrapolate a single data point into a wind field. Following this, at each defined grid point, a
corresponding wind speed value is assigned. The Holland model wind field is computed for each data point available
from IBTrACS, given the data constraints. More information on the Holland model is provided in Section 2.4.



5. **Scale wind speeds to 100 m height:** The Holland model returns wind speeds at gradient height, the height at wind
 90 surface friction no longer significantly affects the wind flow. These winds are scaled down to 100 m. Any newly created data points from using the Holland Model, that now fall over land, are removed. This is discussed in Section 2.5.

6. **Calculate the annual maxima:** The scaled wind fields are separated into yearly groups, and the annual maxima is calculated for each grid point. The annual maxima calculation is described in Section 2.6.

7. **Fit the Gumbel distribution:** From the annual maxima, the Gumbel distribution is fitted to estimate U_{50} at each grid
 95 point. This is the final step in this method, provides a map of U_{50} for each region. The process is also described in Section 2.6.

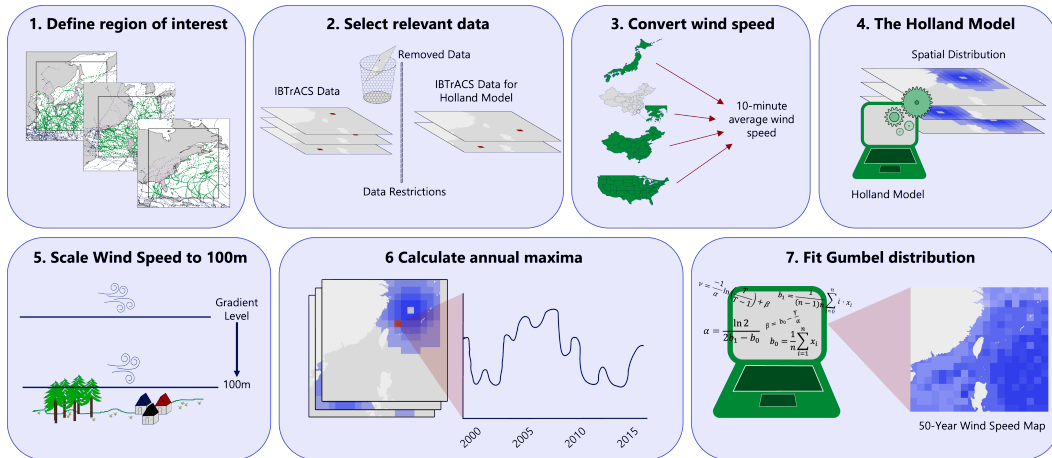


Figure 1. Illustration of seven-step Workflow depicting the method used to calculate U_{50} at 100 m using IBTrACS.

2.1 Data

IBTrACS is a global tropical cyclone dataset maintained by the National Oceanic and Atmospheric Administration (NOAA). NOAA compiles post-storm records of best estimate TC parameters from multiple regional meteorological agencies, providing
 100 information such as storm position, central pressure, and maximum sustained wind speed at regular time intervals (typically every 3 hours). Every 3-hour time step, new values are provided where possible; however, a spatial realisation of the wind field (or other parameters) is not available. IBTrACS serves as a consolidated and quality-controlled reference for historical TC activity. Table 1 shows which agencies' data is available within IBTrACS, in categories of data's temporal resolution; those in bold are used in the following methods in this study. The differences between agencies pose different challenges throughout
 105 the analysis and will be detailed throughout.

Table 2 shows a comparison between the three regions: the time frame of TCs captured for this analysis, the total TCs within each region for the given time frame, the total TCs that have at least one data point with the needed parameters (maximum wind



Table 1. Wind averaging period by agency

1-min wind	2-min wind	3-min wind	10-min wind
US Agencies	China (CMA)	India (IMD)	Japan (JMA)
			Australia (BoM)
			La Reunion
			Fiji (Nadi)
			New Zealand (Wellington)
			Hong Kong (HKO)
			South Korea (KMA)

speed, RMW, minimum sea level pressure) and the number of IBTrACS data points used. Table 3 shows a regional comparison of the grid resolution and the total number of grid points. For the latitude and longitude limits of each region, see Table 4.

Table 2. Regional data comparison

Region	Time frame	Total TCs	Total TCs in analysis	Total IBTrACS data points used
Taiwan	1977-01-01 – 2024-12-26	1004	612	12447
Japan	1977-01-01 – 2024-12-26	819	608	13795
ECUS	2001-01-01 – 2024-12-26	239	214	4990

Table 3. Regional grid comparison

Region	Grid resolution (latitude × longitude)	Total grid points
Taiwan	0.25° × 0.25°	7396
Japan	0.25° × 0.25°	19596
ECUS	0.25° × 0.25°	17892

110 2.2 Defining the “regions”

While three regions are being evaluated within this study: Taiwan, Japan and ECUS, the primary focus is the coastal areas, as this is where most offshore structures are located (e.g., Díaz and Guedes Soares (2020)). Given that TCs can be very intense systems the TC extreme winds can still have a significant impact on areas hundreds of kilometres away from the eye, and therefore, there needs to be consideration of the region chosen. The exact extent of how far damaging winds can reach is a complex subject (Weatherford and Gray, 1988; Powell and Reinhold, 2007; Chan and Chan, 2012; Knaff et al., 2021). To ensure all potential TC effects are captured, a wide area has been chosen to evaluate, as shown by Fig.s 2a, 2b, and 2c. Within these figures, a subset of IBTrACS data is shown to illustrate which IBTrACS data points are included in our calculation. A region of approximately 500 km from the most Northern, Eastern, Western and Southern points are included within the map as



120 shown by the black square. Any data points outside of the black box have been excluded; represented as dark blue dots in the figure. The purple dots over land are also excluded from this study. The green dots represent included data points. The exact coordinate boundaries for each region are listed in Table 4.

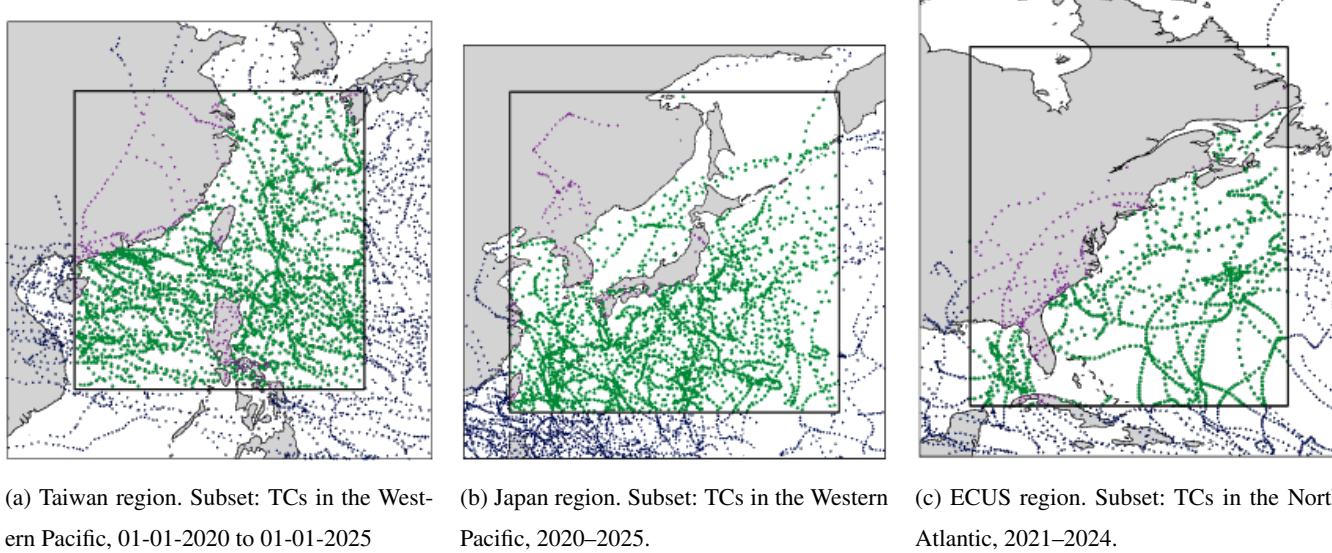


Figure 2. Coordinate restrictions and removed data points for each region. The inner black box represents the coordinate restrictions placed on the IBTrACS data. The dark blue dots represent excluded data points due to being outside the coordinate. The purple dots represent excluded data points due to being over land. The green dots represent data points included in the analysis. Only a subset of IBTrACS data is shown to illustrate which data is excluded.

Table 4. Coordinate restrictions for regions

	Taiwan	Japan	ECUS
Latitude min (degrees)	12° N	21° N	22° N
Latitude max (degrees)	35° N	55,5° N	57,5° N
Longitude min (degrees)	110° W	120,5° W	-88,5° W
Longitude max (degrees)	131,5° W	156° W	-57° W

125 For the ECUS region, data has been used from the pre-compiled US agencies' variables within IBTrACS. All data for the Taiwan region comes from the World Meteorological Organisation Regional Specialised Meteorological Centre in Tokyo. It is operated by the Japanese Meteorological Agency (JMA) responsible for official typhoon forecasts in the western North Pacific. The JMA dataset spans from 1951 to the present. For the Japan region, data from four agencies were combined to maximise the data availability. As previously mentioned, certain parameters are needed, and therefore, merging data from different agencies can help to fill data gaps. A hierarchy of preference was established: JMA, HKO, CMA, US. This order of preference is based



on the number of available data points for the Japan region, with JMA offering the highest count of data points and the US agencies the least.

130 **2.3 Wind Speed Conversion**

Different agencies report the maximum wind speed of TCs using different averaging periods. To ensure consistency across datasets, all wind speeds have been standardised to a 10-minute average to align with IEC standard 61400-1. Shorter averaging periods tend to return higher wind speeds, whereas a longer averaging period results in lower wind speeds as fluctuations of turbulence are smoothed over time. Harper et al. (2010) derived algorithms to convert wind speeds measured at 10 m between 135 different averaging periods. The conversion factors used here are provided in Table 5. The recommended procedure to convert a shorter averaging period to a lower averaging period is as follows:

The wind speed conversion factor (CF) for converting x minute wind speed to y minute wind speed, where $x < y$, is given by:

$$CF = \frac{G_{y,3600}}{G_{x,3600}}$$

140 where $G_{x,3600}$ is a conversion value which gives the highest x second mean (gust) wind speed (for example, 600 seconds - 10 minutes) within 3600 seconds.

Table 5. Wind speed conversion between temporal resolutions of 1 minute to 10 minutes, and 2 minutes to 10 minutes

	Conversion formula	At-Sea
1 minute to 10 minutes	$\frac{G_{600,3600}}{G_{60,3600}}$	$\frac{1.03}{1.11} = 0.93$
2 minutes to 10 minutes	$\frac{G_{600,3600}}{G_{120,3600}}$	$\frac{1.03}{1.07} = 0.96$

2.4 Holland Model

The Holland model, developed by Holland (1980), is a conceptual, empirical model to extrapolate one point of data into a wind field. Figure 3 illustrates a singular data point being extrapolated to an entire wind field. The following use of the Holland 145 model follows the method in Ott (2006). First, the B parameter is calculated:

$$B = \left(\frac{V_{\max}}{K_M} \right)^2 \cdot \rho \cdot e \cdot \frac{1}{(P_n - P_c)} \quad (1)$$

where P_n is the minimum sea level pressure, P_c is the ambient pressure, ρ is air density, V_{\max} is the maximum wind speed at 10 m, e is Euler's number, and the constant $K_m \approx 0.7$.

Using the B parameter, the gradient wind speed can be calculated at distance r from the TC centre:

$$150 \quad V_g = \sqrt{\frac{P_n - P_c}{\rho} \cdot B \cdot \left(\frac{R_0}{r} \right)^B} \cdot \exp \left(-\frac{\left(\frac{R_0}{r} \right)^B}{2} \right) \quad (2)$$



where R_0 is the RMW.

The RMW parameter is collected only by US agencies. Prior to 2001, the data availability of this parameter was limited to at most seven data points per year, restricting the use of the US data to be from 2001 onwards.

The JMA dataset does not provide the RMW, but the 50 kt radius is provided. Specifically, the longest and shortest radii for 155 50 kt winds are reported, from which the RMW can be estimated. This data is available from 1977 onward. The JMA dataset only covers the Western North Pacific, and the 50 kt radii is not available for the ECUS region.

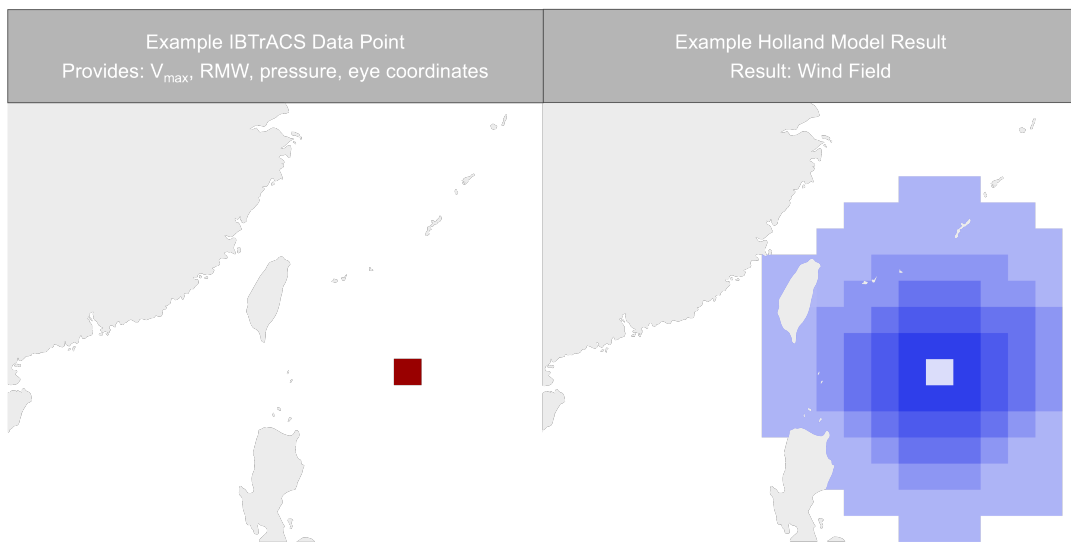


Figure 3. Illustration depicting an example data point from the IBTrACS dataset and the wind field result from using the parameters from the data point as an input into the Holland Model.

2.5 Height scaling for wind

The Holland model outputs wind speed at gradient level (Holland, 1980); the height at which surface friction no longer significantly affects the wind flow. Therefore, the wind speed needs to be scaled to a height that is of use. For this paper, the wind 160 speed has been scaled to 100 m. Franklin et al. (2003) suggests that, for TCs, the layer below the broad maximum wind speed of 500 m, approximately follows the logarithm of the altitude. To scale the wind, firstly, the geostrophic drag law is solved for the friction velocity (Rossby and Montgomery, 1935; Blackadar and Tennekes, 1968):

$$G = \frac{u_*}{\kappa} \sqrt{\left(\ln \left(\frac{u_*}{f_{col} \cdot z_0} \right) - A \right)^2 + C^2} \quad (3)$$

where u_* is the friction velocity, G is the geostrophic wind, κ is the con Kármán constant, f_{col} is the Coriolis parameter, z_0 is 165 the surface roughness length and A and C are constants defined by the neutral conditions. The constants are set as $A = 1.8$ and



$C = 4.5$. Using the friction velocity, the wind speed is scaled to a different height using the logarithmic wind law:

$$u(z) = \frac{u_*}{\kappa} \ln \frac{z}{z_0} \quad (4)$$

where z is the target height. Combining the geostrophic wind law with the logarithmic profile of the wind is a well-established method and already implemented into systems such as Wind Atlas Analysis and Application Program (WAsP) (Troen and Petersen, 1989).

The wind speeds were originally scaled to 10 m for comparison against the IBTrACS dataset. The approach was performed for varying roughness lengths for each region. The optimal roughness length was selected by evaluating, on average, how well the scaled wind speeds match the 10 m IBTrACS data. The adjusted values for the roughness length identified are $5e^{-6}$ m, $9e^{-6}$ m and $1e^{-5}$ m for the Taiwan, Japan and ECUS regions, respectively. Note that these are not actual roughness length, rather values that provide the scaled wind speed from the gradient height to 10 m, matching the 10-m IBTrACS data.

The commonly accepted deep ocean surface roughness value is 0.2 mm (He et al., 2021). However, Ott (2006) shows that the eyewall profile follows the logarithm of the altitude using a surface roughness of 0.07 mm.

To scale to 100 m, the same method was performed using the adjusted roughness length.

2.6 The Gumbel Distribution

For each individual grid point and for each year, the maximum wind speed at 100 m is obtained following Section 2.4 and 2.5. Using the annual maxima, the Gumbel distribution estimates U_{50} . This method follows the approach described in (Abild, 1994; Larsén et al., 2015) in which \mathbf{X}_m is the ascending sorted annual maxima (for each grid point), with n samples.

The sample mean is computed:

$$b_0 = \frac{1}{n} \sum_{i=1}^n X_{m,i} \quad (5)$$

and the weighted mean

$$b_1 = \frac{1}{(n-1)n} \sum_{i=1}^n (i-1) \cdot X_{m,i} \quad (6)$$

The Gumbel distribution parameters α and β can be calculated such that:

$$\alpha = \frac{\ln 2}{2b_1 - b_0} \text{ and } \beta = b_0 - \frac{\gamma}{\alpha} \quad (7)$$

where γ is Euler's constant = 0.57721. The wind speed for the return period T is

$$U_T = -\frac{1}{\alpha} \ln \left(\ln \left(\frac{T}{T-1} \right) \right) + \beta \quad (8)$$

and the standard deviation associated with the wind speed for the return period T is

$$\sigma_T = \frac{\pi}{\alpha \sqrt{6n}} \sqrt{1 + 1.14 k_T + 1.1 k_T^2}. \quad (9)$$

where $k_T = \frac{\sqrt{6}}{\pi} \left(-\ln \left(\ln \left(\frac{T_{\text{return}}}{T_{\text{return}}-1} \right) \right) - 0.577 \right)$



3 Results

195 The results of calculating U_{50} are presented in three regions: Taiwan, Japan and ECUS regions are shown here. Each region will be discussed individually.

3.1 Taiwan

In Figure 4a, U_{50} at 100 m is presented for the Taiwan region. The region expands from latitude $12^{\circ}N$ to $33.5^{\circ}N$ and longitude $110^{\circ}W$ to $131.5^{\circ}W$. Taiwan is located in the centre of the figure, with the Philippines to the south and mainland China to the

200 west.

The highest values of U_{50} are observed east of longitude $120^{\circ}W$, corresponding to areas east of Taiwan and the Philippines. In contrast, in the west of Taiwan and the Philippines, the wind speed is slower by approximately $10 - 20 \text{ m s}^{-1}$. The majority of TCs forming in the Western Pacific form to the south-east of Taiwan (Guo et al., 2025), where they can intensify before weakening as they approach or move over land (Park et al., 2013). Therefore, it is expected to see the highest winds south-east 205 of Taiwan, before reaching land. The spatial distribution of the wind field looks somewhat consistent with previous studies based on IBTrACS data, such as Ott (2006); Kong et al. (2024). To compare with the results of Ott (2006); Kong et al. (2024), U_{50} at 10 m is also provided here (Fig. 4d). The maximum value of U_{50} at 10 m in this area is 72.7 m s^{-1} , which is 72 m s^{-1} in Ott (2006) and 70.4 m s^{-1} in Kong et al. (2024). Figure 4d here also includes more detailed spatial variability of U_{50} at 10 210 m than Ott (2006) and Kong et al. (2024) due to their larger spatial grid spacing of $1^{\circ} \times 1^{\circ}$. It should be noted that the spatial distribution of Fig 4a and 4d is very similar and the 10 m results simply return smaller values. The detailed spatial distribution of U_{50} at 100 m in this study is similar to the results in Larsén and Ott (2022) (their Figure 7a), which was based on the CFSR reanalysis data with grid spacing of about 40 km, where the values of U_{50} were corrected to an equivalent temporal resolution of 10 min.

The 95% confidence interval calculated using Eq. 9 in connection with the use of Gumbel distribution is shown in Fig. 215 4b. It widens in areas where U_{50} increases, peaking at approximately 15 m s^{-1} , and it narrows to approximately 2 m s^{-1} at the smallest. Note that the 95% confidence interval reflects the variability associated with the fitted Gumbel distribution. Uncertainties for the entire process are discussed in Section 4. Figure 4c shows the number of data points above 19 m s^{-1} from 220 the Holland Model at each grid point. NOAA defines a tropical storm when the 1-minute average winds reach 34 kt at 10 m. By converting 34 kt to m s^{-1} , a 10-minute average and scaling the wind speed height to 100 m, the threshold becomes 19 m s^{-1} . These methods are all described in Section 2.

3.2 Japan

In Figure 5a, U_{50} at 100 m is presented for the Japan region. The region expands from latitude $21^{\circ}N$ to $55.5^{\circ}N$ and longitude $120.6^{\circ}W$ to $156^{\circ}W$. Japan is located in the centre of the figure, with South Korea, North Korea, Russia and China located to the west. In this region, the genesis of TCs typically occurs at lower latitudes, and they move in a north-west direction. The 225 Coriolis force turns the TCs further north, and once it has reached mid-latitudes, the TC turns eastward due to westerlies in

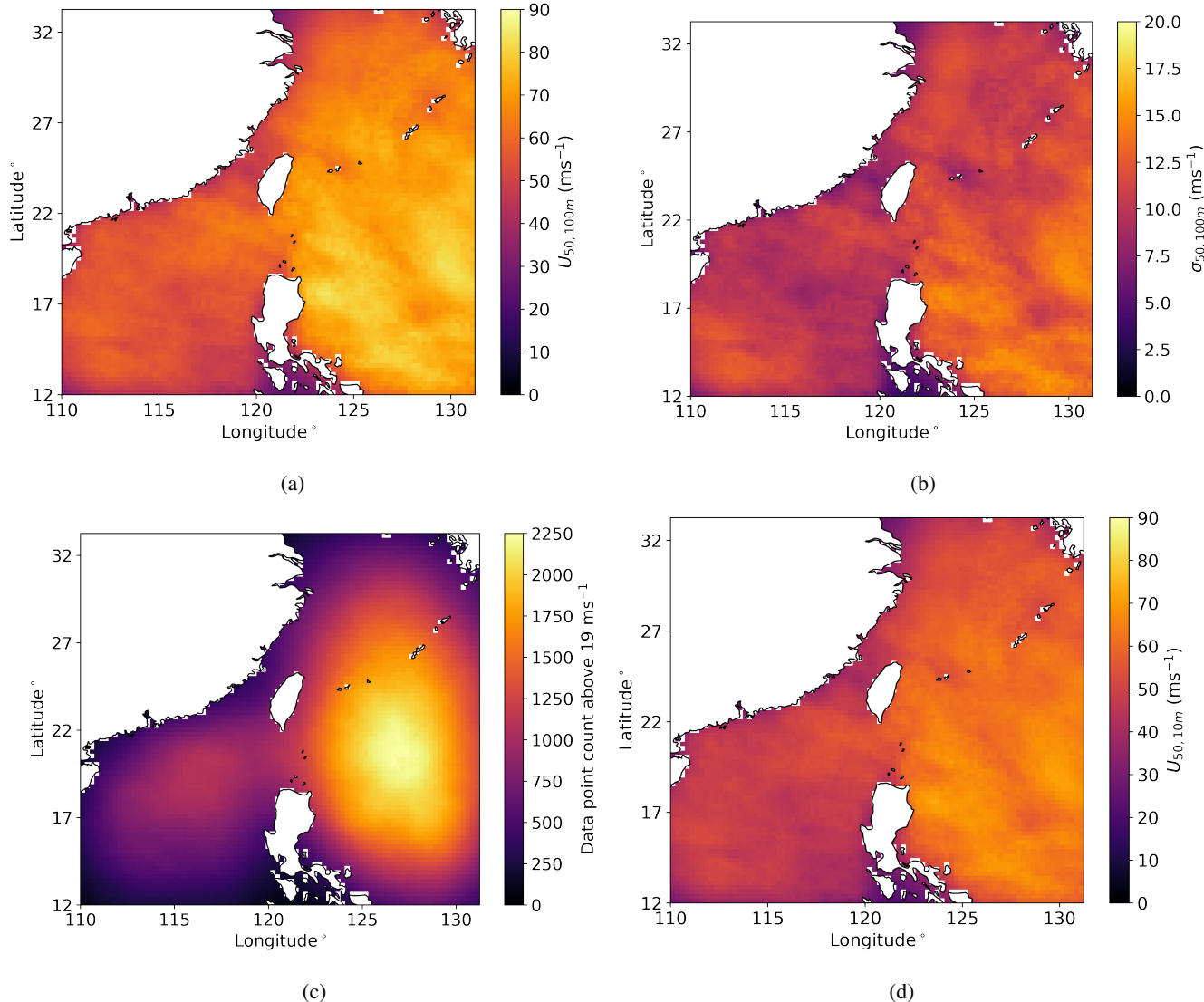


Figure 4. Results for Taiwan. (a): U_{50} at 100 m. (b): The 95% confidence interval from the Gumbel distribution calculated using $1.96 \sigma_{50}$. (c): The number of data points from the Holland model calculation that are equal to or above 19 m s^{-1} . (d): U_{50} at 10 m.

addition to the Coriolis force (Cao et al., 2025). As they move north, the sea water temperature typically becomes cooler and the TC weakens (Fei et al., 2020), hence the higher U_{50} values occurring at latitudes lower than 36°N while the TC still holds intensity. In Figure 5c, showing the number of values each grid point has above 19 m s^{-1} , there are far fewer data points above 36°N degrees latitude in comparison to below 36°N degrees latitude, and above 46°N degrees latitude there are few to no data points giving explanation as to why wind speeds approach 0 m s^{-1} in this region. However, this does not mean that the



extreme wind speed in these areas is negligible, as other weather processes can take place, but this study solely focuses on tropical cyclone extreme wind speed. This clearly demonstrates the uncertainty associated with too few data samples.

The southern coastline of Japan is the most exposed, though both the southwestern and southeastern coastlines still experience elevated wind speeds due to TCs. As in the Taiwan region, the 95% confidence interval increases with wind speed,
 235 reaching its highest values in areas where there is substantial and strong TC activity.

The spatial distribution as well as the magnitude of U_{50} at 100 m in Fig. 5a is quite similar to that in Larsén and Ott (2022) (their Fig. 7a) for the overlapping area, including the patchy patterns. Such levels of detail are absent in Ott (2006) and Kong et al. (2024) due to the coarser spatial resolution.

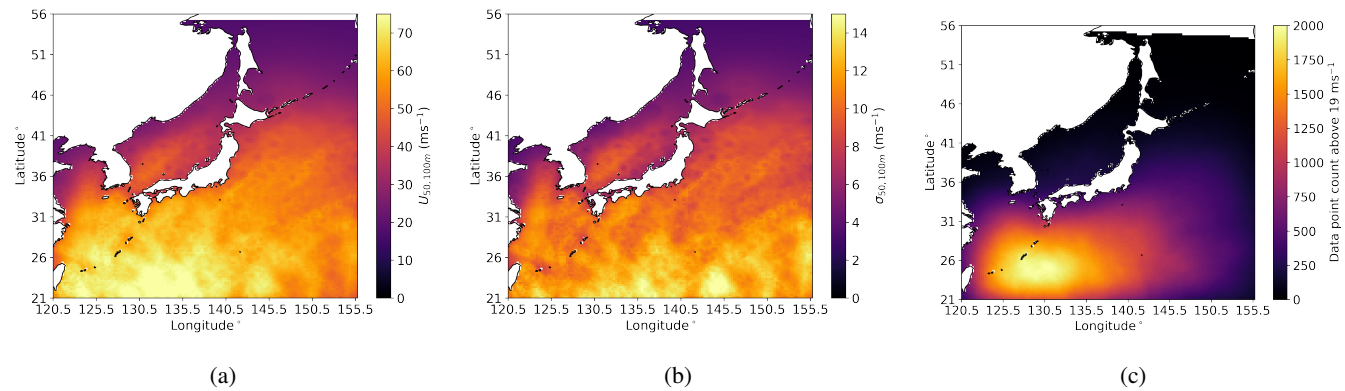


Figure 5. Results for Japan. (a): U_{50} at 100 m. (b) The 95% confidence interval from the Gumbel Distribution calculated using $1.96 \sigma_{50}$. (c): The number of data points from the Holland Model calculation that are equal to or above 19 m s^{-1} .

3.3 East Coast of the United States

240 In Figure 6a, U_{50} at 100 m is presented for the ECUS region. The region expands from latitude $22^\circ N$ to $57.5^\circ N$ and longitude $-88.5^\circ W$ to $-57^\circ W$. The east coast of the United States of America is shown, along with the top of the Caribbean in the south.

The results from the ECUS region deviate from expectations. At a granular scale, the eyewall of the TC is evident as it traverses over the region, and the U_{50} field exhibits a fragmented structure, which will be discussed in Section 5. On a macro scale, the spatial distribution of U_{50} maxima and minima is unexpected. The highest wind speeds were anticipated to occur
 245 consistently within the lower half of the region. This distribution was expected due to the positive correlation between latitude and RMW (Kimball and Mulekar, 2004; Vickery and Wadhera, 2008; Pérez-Alarcón et al., 2021) and TCs within the Gulf of Mexico, on average, have a smaller RMW than those in the Atlantic (Vickery and Wadhera, 2008). The intensity of a TC is inversely related to the RMW (Kimball and Mulekar, 2004; Chavas and Knaff, 2022), meaning, on average, storms with smaller RMW tend to have stronger winds than TCs with large RMW.

250 The results here show, that while the highest return level is 74.9 m s^{-1} at $26.75^\circ N$ degrees latitude and $-64.75^\circ W$ degrees longitude, the latitude further north also exhibits return levels which are nearly as high. The wind speeds between latitudes $33^\circ N$ and $40^\circ N$ and longitudes $-64.5^\circ W$ and $-59.5^\circ W$ are noted as rather high.



The 95% confidence intervals follow the same pattern as in the previous cases: regions with higher wind speeds correspond to a widening confidence interval. Furthermore, the confidence interval structure also follows the same structure as U_{50} .

255 The study of Larsén and Ott (2022), reflecting the reanalysis CFSR wind field, does suggest a stronger $U_{50,100m}$ band south of $30^{\circ}N$, between about $(30^{\circ}N, -75^{\circ}W)$ and $(22^{\circ}N, -65^{\circ}W)$, with the highest value of about 73 m s^{-1} . Due to the Coriolis force and westerlies, this strong $U_{50,100m}$ band turns north-east (their Fig. 7c). Compared to Larsén and Ott (2022), Fig. 6a here captured the second, relatively weaker extreme wind band north of $30^{\circ}N$, and did not capture the full picture of the first, stronger extreme wind band. We argue that it is, on one side, caused by the few IBTrACS tracks in this region (see Fig. 6c),
 260 and on the other side, related to the application of the Holland model. The detailed discussion is provided in Section 5. The hotspot in the Caribbean is both present in the current study and in Larsén and Ott (2022).

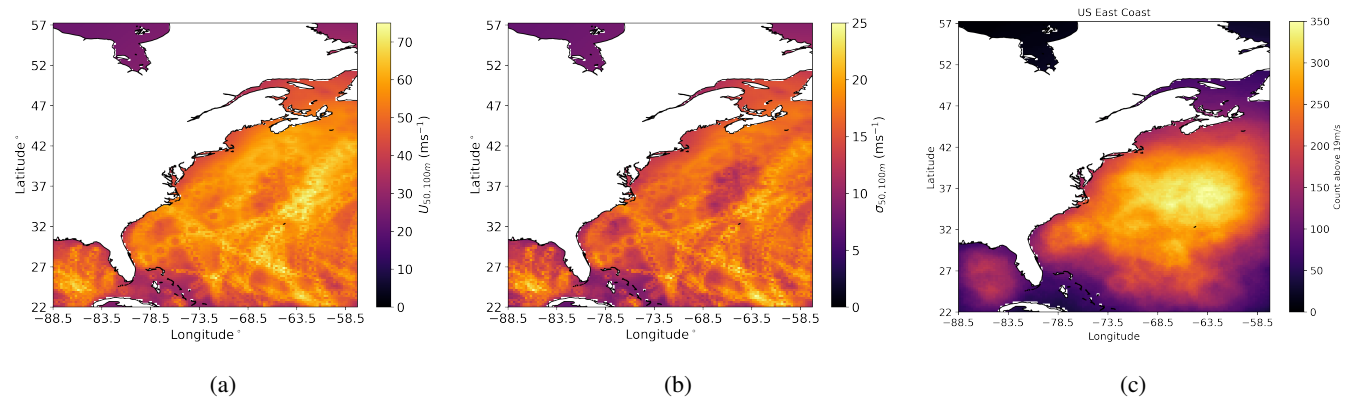


Figure 6. Results for ECUS. (a): U_{50} at 100 m. (b): The 95% confidence interval from the Gumbel Distribution calculated using $1.96 \sigma_{50}$.
 (c): The number of data points from the Holland Model calculation that are equal to or above 19 m s^{-1} .

4 Uncertainty Analysis

As outlined in Section 2, there are several input parameters into the Holland model and the Gumbel distribution, which could introduce uncertainty into the estimation of U_{50} . Given the number of contributing variables, a Monte Carlo (Metropolis and
 265 Ulam, 1949) approach was used to propagate uncertainty throughout the method. The parameters considered include wind speed, centre position, RMW, pressure, the B parameter, and scaled wind speed. Monte Carlo simulations are a common method to estimate uncertainty within the wind energy sector, as shown by Ishihara and Yamaguchi (2015); Yasui et al. (2002);
 Hu et al. (2023)

Most parameters within the uncertainty analysis are sourced from the IBTrACS dataset, and while data from many agencies
 270 are consolidated, the associated errors are not, making the quantification of uncertainty challenging. IBTrACS is typically used as a reference dataset for validation purposes and does not consistently report uncertainty estimates for all variables. Therefore, bespoke methods to quantify each parameter's uncertainty have been used. Some parameters have a uniform range defined,



others require comparison of values from various agencies for a standard deviation to be calculated, and one requires error propagation.

275 Here in the Monte Carlo framework, each parameter was randomly sampled within an estimated 95% confidence interval using $\pm 1.96\sigma$, allowing comparisons across parameters. The method was repeated 100 times for each parameter. The following section outlines the approach taken to estimate the uncertainty for each variable.

4.1 Uncertainty associated with key parameters

4.1.1 Wind Speed

280 Wind speed is one of the few parameters for which uncertainties are provided within the IBTrACS documentation (IBTrACS Science Team, 2025), shown below in Table 6. As noted by the IBTrACS documentation, the uncertainty estimates are calculated from the contributions from the 3rd IBTrACS Workshop attendees. It takes into account the changes of forecasting methods over the year, changes in aircraft reconnaissance in the Western Pacific and Northern Atlantic and information provided from more than one agency for several basins. The absolute uncertainties change based on both year and ocean basin and
285 are noted to be qualitative in nature.

While the absolute uncertainty is uniformly distributed, for this paper, the error distribution has been approximated as Gaussian, with the half-width, a , being equivalent to 1.96σ . This is a further step of approximation than that from BIPM and IEC and IFCC and ILAC and ISO and IUPAC and IUPAP and OIML (2008), which estimates the standard deviation of a uniform distribution as

$$290 \sigma = \frac{a}{\sqrt{3}} \quad (10)$$

All parameters for which the absolute uncertainty is provided, the same approximation will take place.

Table 6. IBTrACS Wind Speed Uncertainty (Knots)

Year	Northern Atlantic	Western Pacific
1973 - 1978	$\pm 20 \text{ kt}$	$\pm 20 \text{ kt}$
1978 - 1984	$\pm 15 \text{ kt}$	$\pm 20 \text{ kt}$
1984 - 1987	$\pm 10 \text{ kt}$	$\pm 10 \text{ kt}$
1987 - 1995	$\pm 10 \text{ kt}$	$\pm 15 \text{ kt}$
1995 - 2000	$\pm 10 \text{ kt}$	$\pm 10 \text{ kt}$
2000 - present	$\pm 7 \text{ kt}$	$\pm 10 \text{ kt}$

4.1.2 Position

The position refers to the centre latitude-longitude location of a TC. The uncertainty for the position is also available from the IBTrACS documentation and is shown below in Table 7. Following the approximation within Section 4.1.1, the upper range



295 of the absolute uncertainty is approximated as 1.96σ . For example, $1.96\sigma = 40$ km, therefore the latitude and longitude will be varied within ± 40 km from their original position.

Table 7. IBTrACS Position Uncertainty (Kilometres)

Intensity	Uncertainty
Weak TC (Winds < 60 kt)	$\approx 30 - 40$ km
Moderate TC (60 kt < Winds < 100 kt)	$\approx 20 - 25$ km
Strong TC (Winds > 100 kt)	$\approx 10 - 15$ km

4.1.3 RMW

The RMW uncertainty has been calculated differently for the Northern Atlantic, where the ECUS lies, and the Western Pacific, where the Taiwan and Japan regions lie.

300 The ECUS will first be discussed. The US agencies' RMW uncertainty can be found in an online NOAA report <https://www.nhc.noaa.gov/data/hurdat/hurdat2-format-atl-1851-2021.pdf>, and a subset is shown below in Table 8. The report details extra information on the HURDAT2 dataset (Landsea and Franklin, 2013), which is supplied to IBTrACS.

For the ECUS region, only years from 2001 are included. Satellites carrying scatterometers were active for the entire period of analysis. Satellites providing near-global ocean coverage every 1-2 days include: QuikSCAT (1999–2009) (Hoffman and 305 Leidner, 2005), ASCAT on MetOp-A (from 2006) (Figa-Saldaña et al., 2002; Wagner et al., 2013), and MetOp-B/C (from 2012/2018) (Wagner et al., 2013). Regions in which TCs occur are a priority for satellite coverage as many agencies rely on up-to-date coverage of TCs for modelling and accurate short-term forecasts (Kishtawal, 2016). Therefore, the absolute uncertainty was selected to be 12 nautical miles.

Given the approximation within Section 4.1.1, we define the absolute uncertainty, 12 nm equivalent to 1.96σ , and vary the 310 RMW within this range.

Table 8. US agencies IBTrACS Radius of Maximum Wind Uncertainty (Nautical Miles)

Category and data available	Uncertainty
Category 1 or 2 Hurricane - Satellite/no scatterometer within 6 hr	± 16 nm
Category 1 or 2 Hurricane - Satellite/with scatterometer within 6 hr	± 12 nm
Category 1 or 2 Hurricane - Aircraft and satellite	± 9 nm
Category 1 or 2 Hurricane - U.S. landfall	± 8 nm
Category 3, 4, or 5 Hurricane - Satellite/no scatterometer within 6 hr	± 11 nm
Category 3, 4, or 5 Hurricane - Satellite/with scatterometer within 6 hr	± 9 nm
Category 3, 4, or 5 Hurricane - Aircraft and satellite	± 5 nm
Category 3, 4, or 5 Hurricane - U.S. landfall	± 5 nm



For the Western Pacific, the outcome of converting the 50 km radius to the RMW is compared to available values from the US agencies within the Western Pacific region. From the differences, the mean standard deviation was 10567 m.

4.1.4 Pressure

For the Northern Atlantic, Landsea and Franklin (2013) defines the absolute pressure uncertainty as 9.5 hPa for major TCs
315 observed via satellite. For weaker TCs, such as category 1 or 2, the uncertainty is smaller. Therefore, using the uncertainty of 9.5 hPa is likely a conservative approach. Following the approximation within Section 4.1.1, we assign the absolute uncertainty, 9.5 hPa, as equivalent to 1.96σ and vary the pressure value within this range.

Within the Western Pacific, multiple agencies provide pressure values for the same TC time steps. These agencies include the JMA, HKO, CMA and US. Pressure values from these various agencies for each TC and time step were compared against
320 each. The comparisons were used to calculate the mean standard deviation, which returned as 2.13 hPa and set as equivalent to 1.96 σ .

4.1.5 *B* parameter

The *B* parameter is not provided directly in the IBTrACS dataset, but rather calculated from other variables. These variables are the central pressure and the maximum wind speed. As such, there is no documented uncertainty associated with the *B*
325 parameter. To estimate its uncertainty, the error propagation formula for correlated variables is applied:

$$\sigma_b^2 = \left(\frac{\partial b}{\partial V_{\max}} \right)^2 \sigma_{V_{\max}}^2 + \left(\frac{\partial b}{\partial P_c} \right)^2 \sigma_{P_c}^2 + 2 \left(\frac{\partial b}{\partial V_{\max}} \right) \left(\frac{\partial b}{\partial P_c} \right) \text{Cov}(V_{\max}, P_c) \quad (11)$$

This expression is derived from the first-order Taylor expansion, and its general application is described in Taylor (1997), while its application to meteorological contexts is described in detail in BIPM and IEC and IFCC and ILAC and ISO and IUPAC and IUPAP and OIML (2008).

330 The estimation relies on the assumption that the errors are small compared to the mean of the maximum wind speed and the pressure, the errors are unbiased and symmetric, and the errors are independent, or the covariance is accounted for, which is the case here.

In the Western Pacific, the uncertainty in wind speed varies over time, resulting in corresponding temporal variation in the *B*
335 parameter uncertainty. Once the variation in wind speed uncertainty over time is taken into account, for each time period, the mean *B* parameter standard deviation is found and used. In contrast, for ECUS, only data from 2001 onward are used, during which a single wind speed uncertainty value applies. Consequently, a single *B* parameter uncertainty estimate is reported for the ECUS region.

4.1.6 Scaled Wind Speed

The Holland model returns the wind speed at the gradient level. To understand the wind speed impact on offshore infrastructure,
340 the wind speed at a more relevant height should be calculated. The method of scaling the wind height from the gradient level



Table 9. B Parameter Standard Deviation (unitless)

	Northern Atlantic	Western Pacific
1973 - 1984	na	0.6999
1984 - 1987	na	0.3362
1987 - 1995	na	0.5433
1995 - 2001	na	0.3839
2001 - present	0.2444	0.3839

to 100 m is detailed in Section 2.5. For validation, the wind speed was scaled to 10 m and the value was compared against IBTrACS. Using the difference between the two, the standard deviation could be calculated.

Table 10. Scaled Wind Speed Standard Deviation (m s^{-1})

Taiwan	Japan	ECUS
0.0171 m s^{-1}	0.0216 m s^{-1}	0.0393 m s^{-1}

4.1.7 Contributions to Total Uncertainty

To assess the influence of input parameters on the overall uncertainty of U_{50} , a variance-based sensitivity analysis is performed.

345 This captures both individual effects and interaction terms. This approach is an approximation of the first and second order indices of Sobol (2001). Sobol's indices are widely used in sensitivity analysis (Dykes et al., 2014; Locatelli et al., 2017; Thapa and Missoum, 2022; Tsvetkova and Ouarda, 2019), however, this implementation follows a simpler approach: parameters are randomly sampled within their 95% confidence intervals.

Let $x_{p,m,i}$ be the value of parameter p of Monte Carlo simulation m at grid point i . Normalise each value at each grid point for 350 each parameter:

$$\tilde{x}_{p,m,i} = \frac{x_{p,m,i} - \bar{x}_{p,i}}{\bar{x}_{p,i}}, \quad (12)$$

where $\bar{x}_{p,i}$ is the mean of all simulation values for grid point i and parameter p . Firstly, the variation around the mean is calculated using $x_{p,m,i} - \bar{x}_{p,i}$. Following this, the variation is normalised by $\bar{x}_{p,i}$ to find the relative variation. The relative variation is used so that direct comparison can be made between parameters which have different units and scales of magnitude.

355 To calculate the variance (diagonal terms), which represent the individual parameters' contributions to total uncertainty, the following steps are taken:

Firstly, the variance term of parameter p at a singular grid point i is calculated by:

$$\text{Var}_{p,i} = \frac{1}{N} \sum_m \tilde{x}_{p,m,i}^2 \quad (13)$$

where N is the total number of simulations. The total variance from all parameters is defined as



360 $\text{Var}_{\text{diag total}} = \sum_{p,i} \text{Var}_{p,i}$ (14)

To account for the interaction terms, the covariance is computed, showing how parameter uncertainties interact. A positive value indicates that the parameters amplify each other's uncertainty, whereas a negative value indicates that the parameters partially counteract each other's uncertainty. The magnitude of the value indicates how strong this interaction is and how much the interaction contributes to the overall uncertainty. While each Monte Carlo simulation varies a singular parameter at each 365 time, following the completion of the simulations, $\tilde{x}_{p,m,i}$ can be calculated for each parameter at each grid point. This allows the calculation of the covariance term between parameters p_1 and p_2 at a singular grid point i and can be shown as:

$$\text{Cov}_{p_1, p_2, i} = 2 \frac{1}{N} \sum_m \tilde{x}_{p_1, m, i} \tilde{x}_{p_2, m, i} \quad (15)$$

where N is the total number of simulations. The contribution to the total off-diagonal variance from the covariance terms sum over all possible combinations:

370 $\text{Var}_{\text{off-diag total}} = \sum_{\substack{x, y \\ x \neq y}} \sum_i \text{Cov}_{p_x, p_y, i},$ (16)

where $x \neq y$ ensures that only distinct pairs of parameters are considered at each grid point.

The total variance can be defined as the sum of all variance and covariance terms and is 100%.

$$\text{Var}_{\text{total}} = \text{Var}_{\text{diag total}} + \text{Var}_{\text{off-diag total}} \quad (17)$$

To calculate the percentage of total variation that each individual parameter and each interaction contributes towards is 375 calculated by summing the variation for each individual parameter and each interaction across all grid points:

$$\text{Var}_p = \sum_i \text{Var}_{p,i} \quad (18)$$

$$\text{Var}_{p_x, p_y} = \sum_i \text{Cov}_{p_x, p_y, i}, \quad (19)$$

and dividing by the total variation from all parameters and interactions calculated in Equation 17.

4.2 Uncertainty Results

380 The mean U_{50} and the standard deviation were calculated for each parameter for each set of 100 simulations. Each parameter was varied exclusively, while all others were held constant. Each parameter was varied within its approximate 95% confidence interval. The regional results are presented in Fig.s 7, 8 and 9.



As shown in Tables 11, 12 and 13 across all regions, specific individual parameters dominate the overall uncertainty, rather than the interactions, where all parameter interactions contribute below 1% in all cases.

385 The results shown in Tables 11 for Taiwan and 12 for Japan are, as expected, similar. They are close in proximity and have similar data restrictions. In both regions, the B parameter dominates the impact on the overall uncertainty. This could be attributed to the B parameter incorporating the uncertainty of two parameters, leading to a larger combined variance. The RMW has a smaller impact on the Taiwan and Japan regions; however, it contributes significantly to uncertainty within the ECUS region, particularly to the south, which will be further discussed in Section 5. Within the ECUS region, RMW, wind speed and the B parameter have similar uncertainty; however, the method takes into account the entire defined region. From 390 Figure 9, it is clear the RMW uncertainty is primarily heightened in the southern half of the region. By breaking the region down further, the contribution to overall uncertainty would likely shift.

Wind speed uncertainty for all regions has a substantial impact, which is expected given its direct role in the U_{50} calculation. Surprisingly, pressure uncertainty shows little influence in all three regions, suggesting that either the Holland model has 395 low sensitivity to pressure variation or that the uncertainty associated with pressure is minimal. Scaling the wind speed and changing the latitude/longitude of the maximum wind speed appear to have a negligible impact on the overall uncertainty.

Examining the interaction contributions to the total uncertainty in Tables 11, 12 and 13, given that RMW, wind speed, and the B parameter are the biggest individual contributors to uncertainty, it is unsurprising that their interactions are the biggest contributions to uncertainty. Two notable features of the data are observed: (1) the largest interaction is between the RMW and 400 B parameter in Taiwan, accounting for 7.2%; (2) the wind speed and B parameter interaction in Japan is negative, indicating that the uncertainty of these parameters partially counteract each other. However, given the confidence intervals associated with all interaction contributions, these effects could be close to negligible. Therefore, the primary focus should remain on the individual effects.

5 Discussion

405 There have been several methods developed in the literature to estimate the extreme winds in TC-prone areas.

Studies on this subject have previously used the IBTrACS data and covered the western North Pacific Ocean, with the winds at 10 m height, as in Ott (2006); Kong et al. (2024). This study differs from the previous by examining the entire IBTrACS data records from different agencies. The study area not only includes the western North Pacific Ocean, but also the east coast 410 of the US. We examine both the wind speeds at 10 m, in order to compare with previous studies, but primarily wind speeds at 100 m, which is more relevant for modern wind turbines.

In this study, three regions were selected due to relatively high level of activities for offshore wind deployment: Taiwan, Japan and ECUS. Given a set of data restrictions, data from IBTrACS was used as input to the Holland model. The Holland model returned a wind field for each given data point. The wind speed was scaled down to 100 m using an adjusted roughness length. To estimate the adjusted roughness length, the Holland model output was scaled to 10 m and compared against the 415 maximum wind speed from IBTrACS. The surface roughness, which resulted in the best fit to the IBTrACS values, was

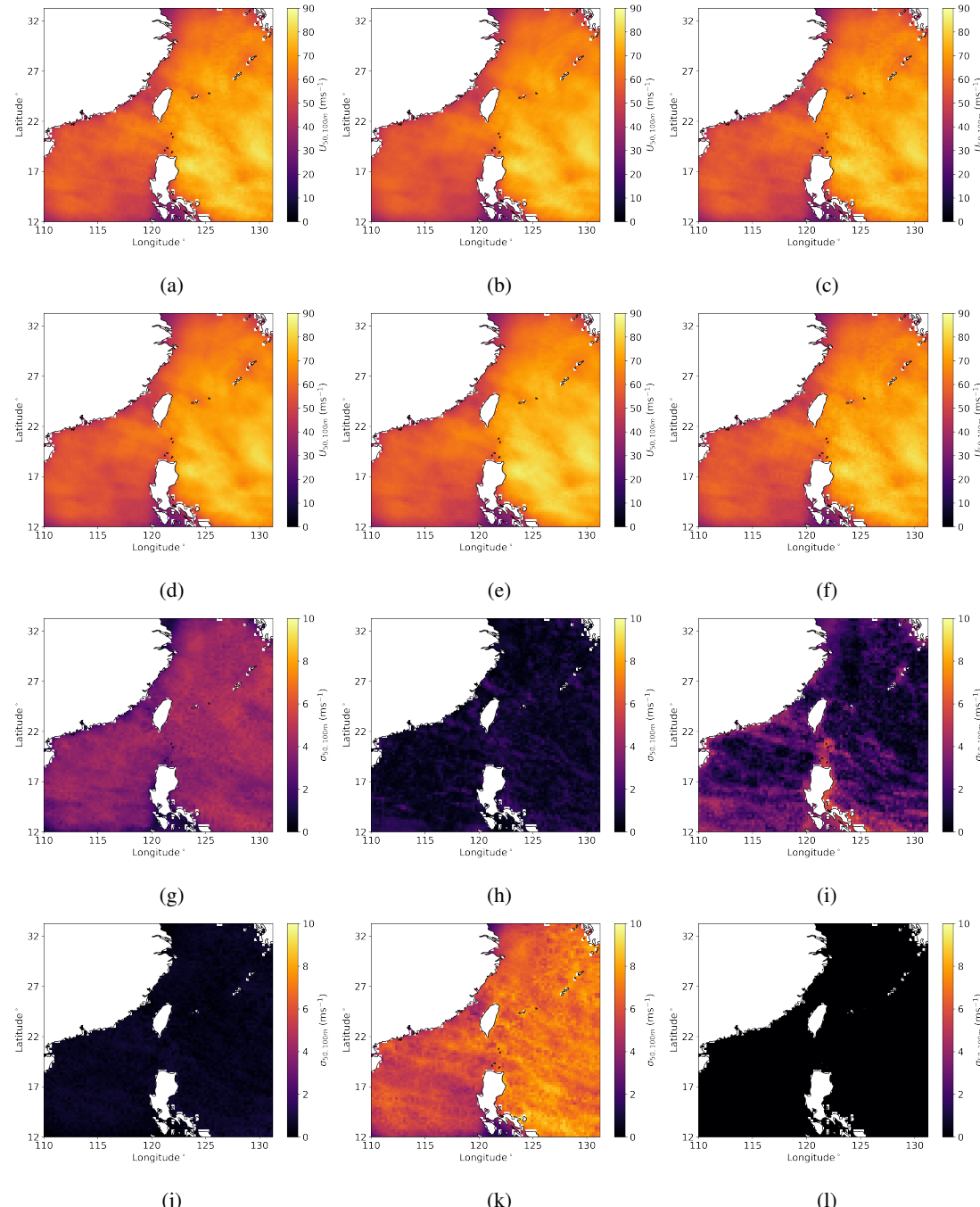


Figure 7. Monte Carlo Simulation results for Taiwan. (a)-(f) shows the mean wind speed from 100 simulations for each varying parameter and (g)-(l) shows the standard deviation from 100 simulations for each varying parameter. (a) and (g): Wind speed. (b) and (h): Eye coordinates. (c) and (i): RMW. (d) and (j): Pressure. (e) and (k): B parameter. (f) and (l): Scaled Wind Speed.

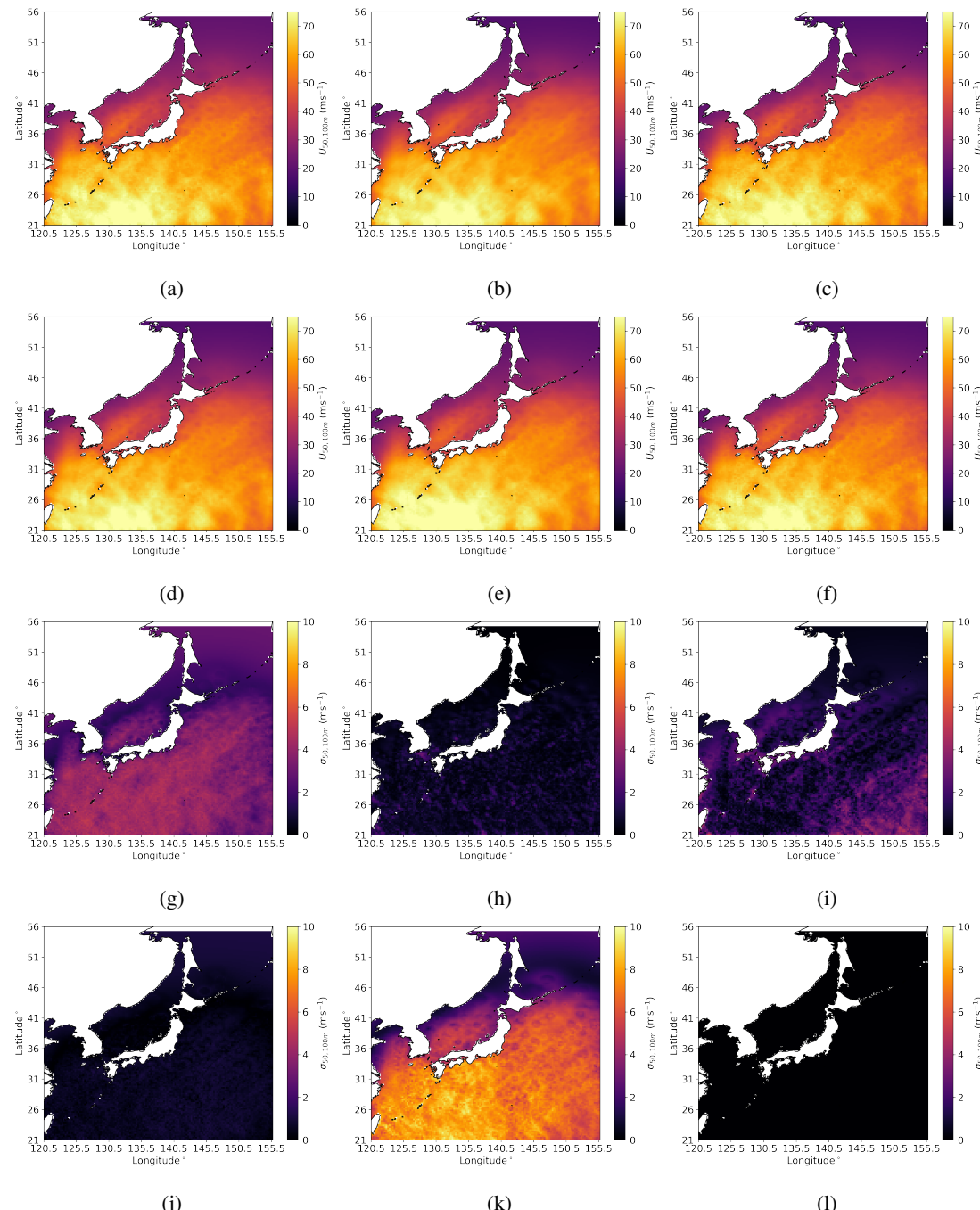


Figure 8. Monte Carlo Simulation results for Japan. (a)-(f) shows the mean wind speed from 100 simulations for each varying parameter and (g)-(l) shows the standard deviation from 100 simulations for each varying parameter. (a) and (g): Wind speed. (b) and (h): Eye coordinates. (c) and (i): RMW. (d) and (j): Pressure. (e) and (k): B parameter. (f) and (l): Scaled Wind Speed.

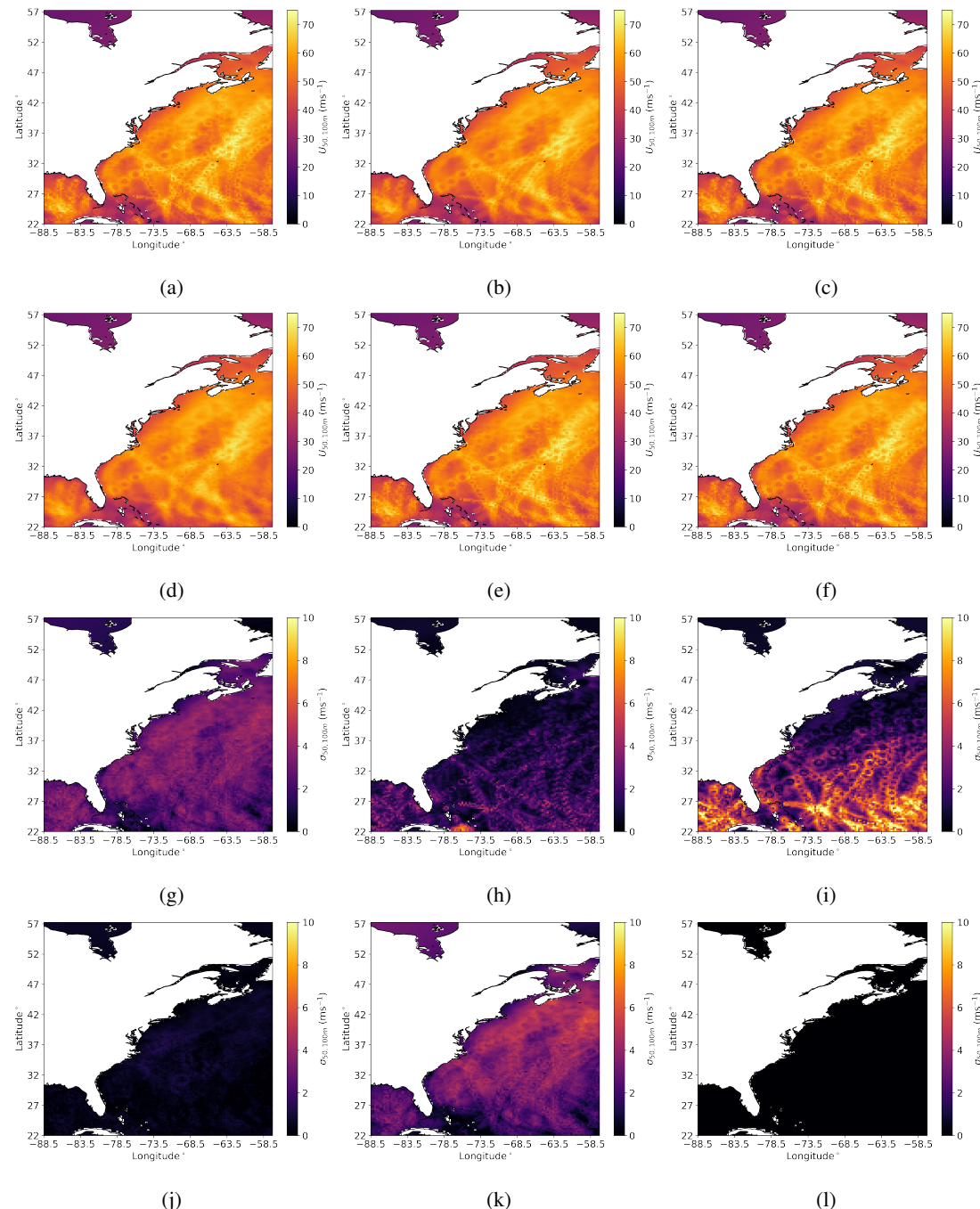


Figure 9. Monte Carlo Simulation results for ECUS. (a)-(f) shows the mean wind speed from 100 simulations for each varying parameter and (g)-(l) shows the standard deviation from 100 simulations for each varying parameter. (a) and (g): Wind speed. (b) and (h): Eye coordinates. (c) and (i): RMW. (d) and (j): Pressure. (e) and (k): B parameter. (f) and (l): Scaled Wind Speed.



Table 11. Contribution to Total Uncertainty in Taiwan (Percentage)

Parameter	Percentage	Std	Interaction	Percentage	Std
Wind Speed	23.0%	7.0%	Position	0.1%	0.7%
			RMW	1.2%	1.0%
			Pressure	0.3%	0.2%
			B Parameter	1.8%	2.4%
			Scaled Wind Speed	0.0%	0.0%
Position	1.2%	1.21%	RMW	-0.3%	0.5%
			Pressure	-0.0%	0.1%
			B Parameter	-0.0%	0.93%
			Scaled Wind Speed	0.0%	0.0%
RMW	8.3%	9.8%	Pressure	0.1%	0.1%
			B Parameter	7.2%	5.1%
			Scaled Wind Speed	0.0%	0.0%
Pressure	0.5%	0.3%	B Parameter	0.7%	0.4%
			Scaled Wind Speed	0.0%	0.0%
B Parameter	56.7%	8.7%	Scaled Wind Speed	0.0%	0.0%
Scaled Wind Speed	0.0%	0.0%			

selected. The standard deviation of the fit was used within the Monte Carlo simulations. As the surface roughness was selected based on comparison against 10 m data, and this study primarily focuses on wind speeds at 100 m, there is potential for further uncertainty to arise, which has not been taken into account. Following the scaling of the wind speed to 100 m, at each grid point, the annual maxima was calculated. Lastly, using the Gumbel distribution, U_{50} was calculated as the final result.

420 Monte Carlo simulations were used for uncertainty analysis, where the parameters including wind speed, position, RMW, pressure, B parameter and scaled wind speed were randomly varied 100 times within their 95% confidence interval range. How well the method performed in each of the regions and the associated errors can be attributed to regional differences in TC characteristics.

The method seemed to work well for the Taiwan region by comparison against other studies. The maximum wind speed 425 of U_{50} at 10 m from this study was 0.7 ms^{-1} larger than that from Ott (2006), 2.3 ms^{-1} larger than Kong et al. (2024) and 0.3 ms^{-1} smaller than that in Larsén and Ott (2022). It also presented a similar spatial distribution of winds in which the maximum winds occur to the north-east of the Philippines, high wind speeds extend north, while gradually weakening towards the south of Japan and weaker wind speeds to the west of the Philippines compare to the east of the Philippines. The three 430 studies previously mentioned also included the Japan region, also showing the peak wind speeds occurring to the south of Japan, gradually weakening as the latitude increases. The ECUS region differed from the previous two by deviating from expectations.



Table 12. Contribution to Total Uncertainty in Japan (Percentage)

Parameter	Percentage	Std	Interaction	Percentage	Std
Wind Speed	29.2%	17.7%	Position	0.4%	1.0%
			RMW	-0.3%	4.7%
			Pressure	-0.3%	1.0%
			B Parameter	-3.4%	3.1%
			Scaled Wind Speed	0.0%	0.0%
Position	1.0%	1.25%	RMW	0.2%	0.6%
			Pressure	-0.1%	0.8%
			B Parameter	-0.2%	1.0%
			Scaled Wind Speed	0.0%	0.0%
			Pressure	-0.0%	0.1%
RMW	6.2%	6.4%	B Parameter	4.5%	4.0%
			Scaled Wind Speed	0.0%	0.0%
			Pressure	0.8%	1.8%
Pressure	2.6%	4.3%	Scaled Wind Speed	0.0%	0.0%
			B Parameter	0.0%	0.0%
B Parameter	59.5%	16.9%	Scaled Wind Speed	0.0%	0.0%
Scaled Wind Speed	0.0%	0.0%			

Here, we discuss the differences between the regions, primarily why the ECUS looks to be less reliable than the other regions.

Firstly, the focus will be on the prominent appearance of specific tracks within the ECUS region in comparison to the much weaker appearance in Japan and Taiwan. By evaluating the data availability of these regions, it becomes apparent that, per year 435 on average, the ECUS region has the least amount of data points, which can be calculated from Table 2. The smaller data count is then coupled with the wider spatial spread of data points, as shown in Fig. 6c. Following this, the ECUS neighbouring grid points can exhibit larger variations in annual maximum wind speeds compared to Japan and Taiwan. In Taiwan and Japan the spatial gradients are generally smoother. The Gumbel distribution is fitted directly to the annual maxima at each grid point, 440 meaning that, the larger differences in annual maxima for neighbouring grid points will produce different U_{50} estimations, causing the fragmented appearance.

Secondly, within the ECUS, it was also expected to see the highest wind speeds consistently appear at lower latitudes due to the correlation of lower latitudes and smaller RMW (Kimball and Mulekar, 2004; Vickery and Wadhera, 2008; Pérez-Alarcón et al., 2021) which indicate stronger winds (Kimball and Mulekar, 2004; Chavas and Knaff, 2022). While this feature is not 445 apparent, it can be explained through examination of the Holland model.

The Holland model is known to underestimate wind speeds at distances two to three times the RMW (Willoughby and Rahn, 2004) as it rapidly decreases the wind speed at these distances. The limitation becomes more pronounced when the RMW



Table 13. Contribution to Total Uncertainty in ECUS (Percentage)

Parameter	Percentage	Std	Interaction	Percentage	Std
Wind Speed	23.5%	11.2%	Position	0.1%	2.1%
			RMW	2.3%	2.2%
			Pressure	0.3%	0.3%
			B Parameter	2.7%	1.6%
			Scaled Wind Speed	0.0%	0.0%
Position	6.94%	8.03%	RMW	0.2%	4.19%
			Pressure	0.0%	0.5%
			B Parameter	0.2%	2.1%
			Scaled Wind Speed	0.0%	0.1%
RMW	31.0%	26.8%	Pressure	0.1%	0.5%
			B Parameter	1.31%	1.61%
			Scaled Wind Speed	0.0%	0.0%
Pressure	1.01%	1.5%	B Parameter	-0.5%	0.7%
			Scaled Wind Speed	0.0%	0.0%
B Parameter	30.8%	20.1%	Scaled Wind Speed	0.0%	0.0%
Scaled Wind Speed	0.0%	0.0%			

is small: the area at two to three times the RMW is still relatively close to the TC's centre, where wind speeds remain high. Therefore, the Holland model's tendency to underestimate winds reduces the accuracy of capturing the extreme wind field from 450 small-RMW TCs. This problem further exacerbates the first issue, which is why at the lower latitudes we see smaller areas of high wind speeds.

In contrast, TCs which track further north in the ECUS region often have larger RMW (Kimball and Mulekar, 2004) and typically have lower maximum wind speeds (Kimball and Mulekar, 2004; Chavas and Knaff, 2022). While the Holland model may still underestimate the wind speeds at two to three times the RMW, this corresponds to a distance much further from 455 the TC's core, where the wind speeds have already weakened. Due to this, the underestimation primarily affects less critical regions of the wind field for this study, while the important core winds are captured reasonably well.

We do not see the spatial fragmentation, to the same extent, occurring within the Taiwan and Japan regions, supporting the theory that the key of the issue is the smaller dataset in the ECUS region. While the underestimation of winds outside two to 460 three times the RMW will still be present, the number of data points in Taiwan and Japan is higher, and it is consolidated into a smaller region in comparison to the ECUS. The annual maxima displays reduced spatial variability between neighbouring points which is reflected in the Gumbel distribution and the U_{50} estimation. Therefore, it is the combination of a smaller dataset in the ECUS than Taiwan and Japan and a consistent area where small-RMW TCs occur that makes this method less reliable for the ECUS region.



465 This rationalisation is supported by the uncertainty analysis. As shown in Figure 9, the RMW within the southern half of the ECUS region plays an important role within the uncertainty, whereas its influence in the Taiwan and Japan regions is much smaller, (Fig.s 7 and 8), even though the same methodology is applied. The larger uncertainty within the Taiwan and Japan regions comes from the B parameters. These differences reflect how regional TC characteristics influence outcomes in each of the regions.

470 Given that many parameters are involved in this method, Monte Carlo simulations were effective to address the associated uncertainty. However, the diversity of uncertainties within the IBTrACS data makes this a challenging analysis. While the uncertainty analysis undertaken in this study may not capture all possible uncertainties, results could provide an indication of the potential range of uncertainty and which parameters affect uncertainty the most.

475 Data availability in the ECUS is heavily limited by the availability of parameter RMW, which is only recorded from 2001 onward. One way to extend the availability is to estimate the RMW using a reanalysis dataset and integrate it with IBTrACS. Another potential option is to use a synthetic dataset, such as STORM (Bloemendaal et al., 2020b) for the analysis. However, this study was intended to specifically focus on IBTrACS data. To better capture the extreme winds from small-RMW TCs, a variation of the Holland model could be used that captures the differences between the inner core and the outer regions, as is suggested by Chavas et al. (2015).

6 Conclusions

480 Overall, this analysis demonstrates that combining IBTrACS data with the Holland model and the Gumbel distribution can provide a viable approach for estimating U_{50} in some TC-affected regions. This approach is most robust in regions with substantial, spatially consolidated datasets and where RMW are not consistently small, such as in Taiwan and Japan. But in regions, like the ECUS, in which the dataset does not fit this criteria, the method shows limitations. Monte Carlo simulations were effective in quantifying uncertainties, highlighting the influence of region specific TC characteristics on the results. While 485 some uncertainties could remain unaccounted for, the approach offers insight into extreme wind estimation at heights relevant for modern wind turbines.

The key findings of this study are summarized as follows:

- The method integrates IBTrACS data, the Holland model, and the Gumbel distribution to estimate extreme wind speeds U_{50} at 10 m and 100 m, complementing previous studies.
- Data for the Taiwan and Japan regions is substantial and consolidated into a specific area allowing for smooth spatial gradients in the annual maxima when comparing neighbouring grid points, leading to more smooth U_{50} estimation across the regions.
- ECUS shows larger variability between neighbouring grid points due to smaller, more widely spread data points which is exacerbated at the lower latitudes due to a higher occurrence of small-RMW TCs.



495 – The Holland model underestimates wind speeds at distances two to three times RMW, particularly affecting small-RMW
TCs and contributing to spatial fragmentation in ECUS.

– Monte Carlo simulations capture the uncertainty from input parameters, though some sources of uncertainty remain
unquantified.

500 *Data availability.* The IBTrACS data is available at <https://www.ncei.noaa.gov/products/international-best-track-archive>, <https://doi.org/10.25921/82ty-9e16> (Gahtan et al., 2024), <https://doi.org/10.1175/2009BAMS2755.1> (Knapp et al., 2010).



References

Abild, J.: Application of the Wind Atlas Method to Extremes of Wind Climatology, Denmark. Forskningscenter Risoe. Risoe-R, Risø National Laboratory, Roskilde, Denmark, ISBN 87-550-1438-0, 1994.

Anastasiades, G. and McSharry, P. E.: Extreme Value Analysis for Estimating 50 Year Return Wind Speeds from Reanalysis Data, Wind Energy, 17, 1231–1245, <https://doi.org/10.1002/we.1630>, 2014.

Arthur, W. C.: A Statistical–Parametric Model of Tropical Cyclones for Hazard Assessment, Natural Hazards and Earth System Sciences, 21, 893–916, <https://doi.org/10.5194/nhess-21-893-2021>, 2021.

BIPM and IEC and IFCC and ILAC and ISO and IUPAC and IUPAP and OIML: Evaluation of Measurement Data — Guide to the Expression of Uncertainty in Measurement, Tech. Rep. JCGM 100:2008, Joint Committee for Guides in Metrology, <https://doi.org/10.59161/JCGM100-2008E>, 2008.

Blackadar, A. K. and Tennekes, H.: Asymptotic Similarity in Neutral Barotropic Planetary Boundary Layers, Journal of the Atmospheric Sciences, 25, 1015–1020, [https://doi.org/10.1175/1520-0469\(1968\)025<1015:ASINBP>2.0.CO;2](https://doi.org/10.1175/1520-0469(1968)025<1015:ASINBP>2.0.CO;2), 1968.

Bloemendaal, N., de Moel, H., Muis, S., Haigh, I. D., and Aerts, J. C. J. H.: Estimation of Global Tropical Cyclone Wind Speed Probabilities Using the STORM Dataset, Scientific Data, 7, 377, <https://doi.org/10.1038/s41597-020-00720-x>, 2020a.

Bloemendaal, N., Haigh, I. D., de Moel, H., Muis, S., Haarsma, R. J., and Aerts, J. C. J. H.: Generation of a Global Synthetic Tropical Cyclone Hazard Dataset Using STORM, Scientific Data, 7, 40, <https://doi.org/10.1038/s41597-020-0381-2>, 2020b.

Cao, X., Wu, R., Jiang, X., Dai, Y., Wang, P., Lin, C., Deng, D., Sun, Y., Wu, L., Chen, S., Wang, Y., and Xiao, X.: Future Changes in Tropical Cyclone Tracks over the Western North Pacific under Climate Change, npj Climate and Atmospheric Science, 8, 148, <https://doi.org/10.1038/s41612-025-01036-6>, 2025.

Chan, K. T. F. and Chan, J. C. L.: Size and Strength of Tropical Cyclones as Inferred from QuikSCAT Data, Monthly Weather Review, 140, 811–824, <https://doi.org/10.1175/MWR-D-10-05062.1>, 2012.

Chavas, D. R. and Knaff, J. A.: A Simple Model for Predicting the Tropical Cyclone Radius of Maximum Wind from Outer Size, Weather and Forecasting, 37, 563–579, <https://doi.org/10.1175/WAF-D-21-0103.1>, 2022.

Chavas, D. R., Lin, N., and Emanuel, K.: A Model for the Complete Radial Structure of the Tropical Cyclone Wind Field. Part I: Comparison with Observed Structure, Journal of the Atmospheric Sciences, 72, 3647–3662, <https://doi.org/10.1175/JAS-D-15-0014.1>, 2015.

Chen, C.-H. and Su, N.-J.: Global Trends and Characteristics of Offshore Wind Farm Research over the Past Three Decades: A Bibliometric Analysis, Journal of Marine Science and Engineering, 10, 1339, <https://doi.org/10.3390/jmse10101339>, 2022.

Commission, I. E.: Design Requirements, Wind Energy Generation Systems / International Electrotechnical Commission, International Electrotechnical Commission, Geneva, Switzerland, edition 4.0 edn., ISBN 978-2-8322-6253-5, 2019.

Díaz, H. and Guedes Soares, C.: Review of the Current Status, Technology and Future Trends of Offshore Wind Farms, Ocean Engineering, 209, 107 381, <https://doi.org/10.1016/j.oceaneng.2020.107381>, 2020.

Dykes, K., Ning, A., King, R., Graf, P., Scott, G., and Veers, P. S.: Sensitivity Analysis of Wind Plant Performance to Key Turbine Design Parameters: A Systems Engineering Approach, in: 32nd ASME Wind Energy Symposium, American Institute of Aeronautics and Astronautics, National Harbor, Maryland, ISBN 978-1-62410-313-1, <https://doi.org/10.2514/6.2014-1087>, 2014.

Fang, P., Ye, G., and Yu, H.: A Parametric Wind Field Model and Its Application in Simulating Historical Typhoons in the Western North Pacific, Journal of Wind Engineering and Industrial Aerodynamics, 199, 104 131, <https://doi.org/10.1016/j.jweia.2020.104131>, 2020.



Fei, R., Xu, J., Wang, Y., and Yang, C.: Factors Affecting the Weakening Rate of Tropical Cyclones over the Western North Pacific, *Monthly Weather Review*, 148, 3693–3712, <https://doi.org/10.1175/MWR-D-19-0356.1>, 2020.

540 Figa-Saldaña, J., Wilson, J. J. W., Attema, E., Gelsthorpe, R., Drinkwater, M. R., and Stoffelen, A.: The Advanced Scatterometer (ASCAT) on the Meteorological Operational (MetOp) Platform: A Follow On for European Wind Scatterometers, *Canadian Journal of Remote Sensing*, 28, 404–412, <https://doi.org/10.5589/m02-035>, 2002.

Franklin, J. L., Black, M. L., and Valde, K.: GPS Dropwindsonde Wind Profiles in Hurricanes and Their Operational Implications, *Weather and Forecasting*, 18, 32–44, [https://doi.org/10.1175/1520-0434\(2003\)018<0032:GDWPIH>2.0.CO;2](https://doi.org/10.1175/1520-0434(2003)018<0032:GDWPIH>2.0.CO;2), 2003.

545 Gahtan, J., Knapp, K. R., Schreck, C. J. I., Diamond, H. J., Kossin, J. P., and Kruk, M. C.: International Best Track Archive for Climate Stewardship (IBTrACS) Project, Version 4.01, <https://www.ncei.noaa.gov/access/metadata/landing-page/bin/iso?id=gov.noaa.ncdc:C01552>, <https://doi.org/10.25921/82ty-9e16>, last Modified: 2024-08-14, NOAA National Centers for Environmental Information, 2024.

Gandoine, R. and Garza, J.: Underestimation of Strong Wind Speeds Offshore in ERA5: Evidence, Discussion and Correction, *Wind Energy Science*, 9, 1727–1745, <https://doi.org/10.5194/wes-9-1727-2024>, 2024.

550 Guo, J., Wang, S., He, X., Song, J., Fu, Y., and Cai, Y.: Interannual Characteristics of Tropical Cyclones in Northwestern Pacific Region in Context of Warm Pool and Monsoon Troughs, *Journal of Marine Science and Engineering*, 13, 334, <https://doi.org/10.3390/jmse13020334>, 2025.

Harper, B. A., Kepert, J. D., and Ginger, J. D.: Guidelines for Converting Between Various Wind Averaging Periods in Tropical Cyclone Conditions, Tech. Rep. WMO-TD-No. 1555, World Meteorological Organization, <https://library.wmo.int/viewer/48652>, 2010.

555 He, Y., Fu, J., Chan, P. W., Li, Q., Shu, Z., and Zhou, K.: Reduced Sea-Surface Roughness Length at a Coastal Site, *Atmosphere*, 12, 991, <https://doi.org/10.3390/atmos12080991>, 2021.

Hoffman, R. N. and Leidner, S. M.: An Introduction to the Near-Real-Time QuikSCAT Data, *Weather and Forecasting*, 20, 476–493, <https://doi.org/10.1175/WAF841.1>, 2005.

Holland, G. J.: An Analytic Model of the Wind and Pressure Profiles in Hurricanes, *Monthly Weather Review*, 108, 1212–1218, [https://doi.org/10.1175/1520-0493\(1980\)108<1212:AAMOTW>2.0.CO;2](https://doi.org/10.1175/1520-0493(1980)108<1212:AAMOTW>2.0.CO;2), 1980.

560 Hu, X., Fang, G., Yang, J., Zhao, L., and Ge, Y.: Simplified Models for Uncertainty Quantification of Extreme Events Using Monte Carlo Technique, *Reliability Engineering & System Safety*, 230, 108935, <https://doi.org/10.1016/j.ress.2022.108935>, 2023.

IBTrACS Science Team: International Best Track Archive for Climate Stewardship (IBTrACS): Technical Documentation (Version 04r01), Tech. rep., NOAA National Centers for Environmental Information, https://www.ncei.noaa.gov/sites/default/files/2025-04/IBTrACS_version4r01_Technical_Details.pdf, accessed: 2025-09-01, 2025.

Imberger, M., Larsén, X. G., and Davis, N.: Global Atlas for Siting Parameters Ocean and Coasts: Ensemble Calculation of 50-Year Return Winds, DTU Wind and Energy Systems E-0244, <https://doi.org/10.11581/DTU.00000321>, 2024.

Ishihara, T. and Yamaguchi, A.: Prediction of the Extreme Wind Speed in the Mixed Climate Region by Using Monte Carlo Simulation and Measure–Correlate–Predict Method, *Wind Energy*, 18, 171–186, <https://doi.org/10.1002/we.1693>, 2015.

570 Kimball, S. K. and Mulekar, M. S.: A 15-Year Climatology of North Atlantic Tropical Cyclones. Part I: Size Parameters, *Journal of Climate*, 17, 3555–3575, [https://doi.org/10.1175/1520-0442\(2004\)017<3555:AYCONA>2.0.CO;2](https://doi.org/10.1175/1520-0442(2004)017<3555:AYCONA>2.0.CO;2), 2004.

Kishtawal, C. M.: Use of Satellite Observations in Tropical Cyclone Studies, in: *Advanced Numerical Modeling and Data Assimilation Techniques for Tropical Cyclone Prediction*, edited by Mohanty, U. C. and Gopalakrishnan, S. G., pp. 35–47, Springer Netherlands, Dordrecht, ISBN 978-94-024-0896-6, https://doi.org/10.5822/978-94-024-0896-6_2, 2016.



575 Knaff, J. A., Sampson, C. R., Kucas, M. E., Slocum, C. J., Brennan, M. J., Meissner, T., Ricciardulli, L., Mouche, A., Reul, N., Morris, M., Chirokova, G., and Caroff, P.: Estimating Tropical Cyclone Surface Winds: Current Status, Emerging Technologies, Historical Evolution, and a Look to the Future, *Tropical Cyclone Research and Review*, 10, 125–150, <https://doi.org/10.1016/j.tcr.2021.09.002>, 2021.

Knapp, K. R., Kruk, M. C., Levinson, D. H., Diamond, H. J., and Neumann, C. J.: The International Best Track Archive for Climate Stewardship (IBTrACS): Unifying Tropical Cyclone Data, *Bulletin of the American Meteorological Society*, 91, 363–376, 580 <https://doi.org/10.1175/2009BAMS2755.1>, 2010.

Kong, L., Zhang, X., Wu, H., and Li, Y.: Estimation of Extreme Wind Speeds with Different Return Periods in the Northwest Pacific, *Meteorological Applications*, 31, e70012, <https://doi.org/10.1002/met.70012>, 2024.

Kossin, J. P.: Validating Atmospheric Reanalysis Data Using Tropical Cyclones as Thermometers, *Bulletin of the American Meteorological Society*, 96, 1089–1096, <https://doi.org/10.1175/BAMS-D-14-00180.1>, 2015.

585 Kossin, J. P.: A Global Slowdown of Tropical-Cyclone Translation Speed, *Nature*, 558, 104–107, <https://doi.org/10.1038/s41586-018-0158-3>, 2018.

Landsea, C. W. and Franklin, J. L.: Atlantic Hurricane Database Uncertainty and Presentation of a New Database Format, *Monthly Weather Review*, 141, 3576–3592, <https://doi.org/10.1175/MWR-D-12-00254.1>, publisher: American Meteorological Society, 2013.

Larsén, X. G. and Ott, S.: Adjusted Spectral Correction Method for Calculating Extreme Winds in Tropical-Cyclone-Affected Water Areas, 590 <https://doi.org/10.5194/wes-7-2457-2022>, 2022.

Larsén, X. G., Mann, J., Rathmann, O., and Jørgensen, H. E.: Uncertainties of the 50-year wind from short time series using generalized extreme value distribution and generalized Pareto distribution, *Wind Energy*, 18, 59–74, <https://doi.org/10.1002/we.1683>, 2015.

Li, J., Tian, Q., Shen, Z., Xu, Y., Yan, Z., Li, M., Zhu, C., Xue, J., Lin, Z., Yang, Y., and Zeng, L.: Fidelity of Global Tropical Cyclone Activity in a New Reanalysis Dataset (CRA40), *Meteorological Applications*, 31, e70009, <https://doi.org/10.1002/met.70009>, 2024.

595 Liu, G., Jiang, S., Zheng, M., Lin, S., Kong, Y., and Zhan, P.: A Global ERA5-based Tropical Cyclone Wind Field Dataset Enhanced by Integrated Parametric Correction Methods, *Scientific Data*, 12, 1429, <https://doi.org/10.1038/s41597-025-05789-w>, 2025.

Locatelli, T., Tarantola, S., Gardiner, B., and Patenaude, G.: Variance-Based Sensitivity Analysis of a Wind Risk Model – Model Behaviour and Lessons for Forest Modelling, *Environmental Modelling & Software*, 87, 84–109, <https://doi.org/10.1016/j.envsoft.2016.10.010>, 2017.

Mavromatis, T.: Evaluation of Reanalysis Data in Meteorological and Climatological Applications: Spatial and Temporal Considerations, 600 <https://doi.org/10.3390/w14172769>, 2022.

Metropolis, N. and Ulam, S.: The Monte Carlo Method, *Journal of the American Statistical Association*, 44, 335–341, <https://doi.org/10.2307/2280232>, 1949.

Morin, G., Boudreault, M., and García-Franco, J. L.: A Global Multi-Source Tropical Cyclone Precipitation (MSTCP) Dataset, *Scientific Data*, 11, 609, <https://doi.org/10.1038/s41597-024-03395-w>, 2024.

605 Mortlock, T. R., Metters, D., Soderholm, J., Maher, J., Lee, S. B., Boughton, G., Stewart, N., Zavadil, E., and Goodwin, I. D.: Extreme Water Levels, Waves and Coastal Impacts During a Severe Tropical Cyclone in Northeastern Australia: A Case Study for Cross-Sector Data Sharing, *Natural Hazards and Earth System Sciences*, 18, 2603–2623, <https://doi.org/10.5194/nhess-18-2603-2018>, 2018.

Ott, S.: Extreme Winds in the Western North Pacific, Denmark. *Forskningscenter Risoe. Risoe-R*, Risø National Laboratory, Roskilde, ISBN 87-550-3500-0, 2006.

610 Park, D.-S. R., Ho, C.-H., Kim, J.-H., and Kim, H.-S.: Spatially Inhomogeneous Trends of Tropical Cyclone Intensity over the Western North Pacific for 1977–2010, *Journal of Climate*, 26, 5088–5101, <https://doi.org/10.1175/JCLI-D-12-00386.1>, 2013.



Powell, M. D. and Reinhold, T. A.: Tropical Cyclone Destructive Potential by Integrated Kinetic Energy, *Bulletin of the American Meteorological Society*, 88, 513–526, <https://doi.org/10.1175/BAMS-88-4-513>, 2007.

Pérez-Alarcón, A., Sorí, R., Fernández-Alvarez, J. C., Nieto, R., and Gimeno, L.: Comparative Climatology of Outer Tropical Cyclone Size
615 Using Radial Wind Profiles, *Weather and Climate Extremes*, 33, 100 366, <https://doi.org/10.1016/j.wace.2021.100366>, 2021.

Rossby, C.-G. and Montgomery, R. B.: The Layer of Frictional Influence in Wind and Ocean Currents, *Physics of Fluids*, <https://hdl.handle.net/1912/1157>, 1935.

Schreck, C. J., Knapp, K. R., and Kossin, J. P.: The Impact of Best Track Discrepancies on Global Tropical Cyclone Climatologies Using
IBTrACS, *Monthly Weather Review*, 142, 3881–3899, <https://doi.org/10.1175/MWR-D-14-00021.1>, 2014.

620 Sobol, I. M.: Global Sensitivity Indices for Nonlinear Mathematical Models and Their Monte Carlo Estimates, *Mathematics and Computers
in Simulation*, 55, 271–280, [https://doi.org/10.1016/S0378-4754\(00\)00270-6](https://doi.org/10.1016/S0378-4754(00)00270-6), 2001.

Taylor, J. R.: An introduction to error analysis: the study of uncertainties in physical measurements, University Science Books, Sausalito,
Calif, second edition. edn., ISBN 0-935702-42-3, 1997.

Thapa, M. and Missoum, S.: Uncertainty Quantification and Global Sensitivity Analysis of Composite Wind Turbine Blades, *Reliability
625 Engineering & System Safety*, 222, 108 354, <https://doi.org/10.1016/j.ress.2022.108354>, 2022.

Troen, I. and Petersen, E. L.: European Wind Atlas, Risø National Laboratory, Roskilde, ISBN 978-87-550-1482-4, 1989.

Tsvetkova, O. and Ouarda, T. B. M. J.: Quasi-Monte Carlo Technique in Global Sensitivity Analysis of Wind Resource Assessment with a
Study on UAE, *Journal of Renewable and Sustainable Energy*, 11, 053 303, <https://doi.org/10.1063/1.5120035>, 2019.

Vickery, P. J. and Wadhera, D.: Statistical Models of Holland Pressure Profile Parameter and Radius to Maximum Winds of
630 Hurricanes from Flight-Level Pressure and H*Wind Data, *Journal of Applied Meteorology and Climatology*, 47, 2497–2517,
<https://doi.org/10.1175/2008JAMC1837.1>, 2008.

Vickery, P. J., Wadhera, D., Twisdale, L. A., and Lavelle, F. M.: U.S. Hurricane Wind Speed Risk and Uncertainty, *Journal of Structural
Engineering*, 135, 301–320, [https://doi.org/10.1061/\(ASCE\)0733-9445\(2009\)135:3\(301\)](https://doi.org/10.1061/(ASCE)0733-9445(2009)135:3(301)), 2009.

635 Wagner, W., Hahn, S., Kidd, R., Melzer, T., Bartalis, Z., Hasenauer, S., Figa-Saldaña, J., de Rosnay, P., Jann, A., Schneider, S., Komma,
J., Kubu, G., Brugger, K., Aubrecht, C., Züger, J., Gangkofner, U., Kienberger, S., Brocca, L., Wang, Y., Blöschl, G., Eitzinger, J., and
Steinnocher, K.: The ASCAT Soil Moisture Product: A Review of its Specifications, Validation Results, and Emerging Applications,
Meteorologische Zeitschrift, 22, 5–33, <https://doi.org/10.1127/0941-2948/2013/0399>, 2013.

Wang, Y., Wu, X., Jiang, L., Zheng, F., and Brune, S.: Editorial: Recent Advances in Climate Reanalysis, *Frontiers in Climate*, 5,
<https://doi.org/10.3389/fclim.2023.1158244>, 2023.

640 Weatherford, C. L. and Gray, W. M.: Typhoon Structure as Revealed by Aircraft Reconnaissance. Part II: Structural Variability, *Monthly
Weather Review*, 116, 1044–1056, [https://doi.org/10.1175/1520-0493\(1988\)116<1044:TSARBA>2.0.CO;2](https://doi.org/10.1175/1520-0493(1988)116<1044:TSARBA>2.0.CO;2), 1988.

Wei, M., Fang, G., Zhao, L., Wang, Z., Wang, J., Cao, S., and Ge, Y.: Comparative Study of Typhoon Wind Hazard Estimation in Coastal
Region of China Using Different Wind Field Parameter Models, *Journal of Wind Engineering and Industrial Aerodynamics*, 236, 105 398,
<https://doi.org/10.1016/j.jweia.2023.105398>, 2023.

645 Willoughby, H. E. and Rahn, M. E.: Parametric Representation of the Primary Hurricane Vortex. Part I: Observations and Evaluation of the
Holland (1980) Model, *Monthly Weather Review*, 132, 3033–3048, <https://doi.org/10.1175/MWR2831.1>, 2004.

Xu, Z., Guo, J., Zhang, G., Ye, Y., Zhao, H., and Chen, H.: Global Tropical Cyclone Size and Intensity Reconstruction Dataset for 1959–2022
Based on IBTrACS and ERA5 Data, *Earth System Science Data*, 16, 5753–5766, <https://doi.org/10.5194/essd-16-5753-2024>, 2024.



Yasui, H., Ohkuma, T., Marukawa, H., and Katagiri, J.: Study on Evaluation Time in Typhoon Simulation Based on Monte Carlo Method,
 650 Journal of Wind Engineering and Industrial Aerodynamics, 90, 1529–1540, [https://doi.org/10.1016/S0167-6105\(02\)00268-4](https://doi.org/10.1016/S0167-6105(02)00268-4), 2002.

Appendix A: Appendix A

Table A1. Abbreviation

Abbreviation	Full Name
CFSR	Climate Forecast System Reanalysis
CMA	China Meteorological Administration
ECUS	East Coast of the United States
ERA5	European Centre for Medium-Range Weather Forecast Reanalysis v5
IBTrACS	International Best Track Archive for Climate Stewardship
IEC	International Electrotechnical Commission
JMA	Japan Meteorological Agency
JKO	Hong Kong Observatory
MERRA2	Modern-Era Retrospective analysis for Research and Applications
NOAA	National Oceanic and Atmospheric Administration
RMW	Radius of Maximum Winds
TC	Tropical Cyclone
US	United States

Author contributions. KCS and XGL planned the study, KCS developed the method with input from XGL and MLB. KCS wrote the manuscript draft, and XGL and MLB reviewed and edited the manuscript.

Competing interests. No competing interests are present.

655 *Acknowledgements.* This project is funded by the European Union Horizon Europe MSCA Doctoral Network (HORIZON-MSCA-2022-
DN-01-01, grant no. 101119550). The authors acknowledge the IBTrACS data availability (DOI: 10.1175/2009BAMS2755.1). We thank
Jana Fischereit and Niels Morten from DTU for their support. We further thank Søren Ott from DTU for his help and discussions. AI tools
have been used to partially aid the writing of code to process the data and the formulation of some sentences within this paper.